



저작자표시-비영리-변경금지 2.0 대한민국

이용자는 아래의 조건을 따르는 경우에 한하여 자유롭게

- 이 저작물을 복제, 배포, 전송, 전시, 공연 및 방송할 수 있습니다.

다음과 같은 조건을 따라야 합니다:



저작자표시. 귀하는 원저작자를 표시하여야 합니다.



비영리. 귀하는 이 저작물을 영리 목적으로 이용할 수 없습니다.



변경금지. 귀하는 이 저작물을 개작, 변형 또는 가공할 수 없습니다.

- 귀하는, 이 저작물의 재이용이나 배포의 경우, 이 저작물에 적용된 이용허락조건을 명확하게 나타내어야 합니다.
- 저작권자로부터 별도의 허가를 받으면 이러한 조건들은 적용되지 않습니다.

저작권법에 따른 이용자의 권리는 위의 내용에 의하여 영향을 받지 않습니다.

이것은 [이용허락규약\(Legal Code\)](#)을 이해하기 쉽게 요약한 것입니다.

[Disclaimer](#)

Master's Thesis

Investigation of Surface Conduction-driven
Ion Transport in Non-uniform Micro/nanofluidic
Channel Networks

비균일 마이크로/나노채널 네트워크에서의
표면 전도 이온 전달

February 2021

Department of Electrical and Computer Engineering
College of Engineering
Seoul National University

Seoyun Sohn

Investigation of Surface Conduction-driven Ion
Transport in Non-uniform Micro/nanofluidic
Channel Networks


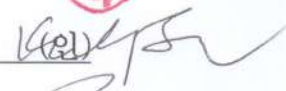

지도교수 김 성 재
이 논문을 공학석사 학위논문으로 제출함

2020 년 9 월

서울대학교 대학원
전기·정보공학부
손 서 윤

손서윤의 공학석사 학위논문을 인준함

2020 년 9 월

위 원 장 홍 용 택 (인) 
부 위 원 장 김 성 재 (인) 
위 원 이 종 호 (인) 

Abstract

Ionic current through a microchannel has drawn significant attention not only for fundamental electrokinetic researches but also for the development of novel micro/nanofluidic applications. Among various ion transport mechanisms, surface conduction, which is a predominant mechanism in micro/nanofluidic devices, has been theoretically characterized based on two-dimensional analyses. However, its infinite axis assumption has become a barrier for being directly applicable in practical micro/nanochannel networks. In this work, we conducted rigorous experiments to include all three-dimensional length scales. There, L/A , the perimeter-to-area ratio of the microchannel cross-section, came up as a single parameter to quantitatively interpret the surface conductive ion transportation. Overlimiting conductance of the devices increased with a larger perimeter, which is equivalent to a specific surface area, even with the same cross-sectional area. A micro/nanofluidic diode with different L/A values on its forward and reverse channel was demonstrated as a simple application. Furthermore, the stability of the overlimiting current was experimentally investigated in connected geometries. Accumulation of particles or byproducts formed inside a fluidic compartment may cause irreversible failure in a flow-based system. In particular, when the feed water contains calcium ions as in natural seawater, calcium hydroxide can form crystals that can grow up to the size of the fluidic channel, which eventually blocks the current path. It was demonstrated in this part that such crystallization is effectively controlled when a geometrical non-uniformity is installed into a microchannel network. Compared to the uniform arrays of parallel microchannels, recirculation flow was enhanced in a predictable pattern when the microchannels have a non-uniform variation in their width. The flow loops induced between the microchannels minimized local ion concentration which feeds the crystals thus the system gained current stability. Presenting analysis would provide a practical guideline to design a micro/nanofluidic application and to passively control the inter-microchannel flow to guarantee the operational life of fluidic systems.

Keywords : Ion concentration polarization, Surface conduction, Non-uniformity, Anti-crystallization.

Student Number : 2018-20846

Table of Contents

Abstract	i
List of Figures	iv
List of Table	v
1. Introduction	1
1.1. Research Background	1
1.1.1. Electrical double layer (EDL)	1
1.1.2. Ion concentration polarization (ICP)	2
1.1.3. Limiting and overlimiting current	5
1.2. Motivation and purpose of the research	8
1.3. Outline of dissertation	9
2. Surface conduction in a microchannel	10
2.1. Introduction	10
2.2. Experimental details	11
2.2.1. Device fabrication and materials	11
2.2.2. Experimental setups	11
2.3. Results and discussion	14
2.3.1. Experimental Designs	14
2.3.2. Ohmic-limiting-overlimiting current measurements	14
2.3.3. 2D analysis vs 3D analysis	19
2.4. Application for nanofluidic diode	20
2.5. Conclusions	21
3. Prevention of undesirable crystallization in non-uniform microchannel networks	22
3.1. Introduction	22
3.2. Experimental details	22
3.2.1. Device fabrication and materials	22
3.2.2. Microchannel designs	23

3.2.3. Experimental setups	23
3.3. Results and discussion	25
3.3.1. Visualization of recirculation flow	25
3.3.2. Current responses and microscopic observation	26
3.3.3. Discussion	28
3.4. Conclusions	29
4. Concluding remarks	30
Bibliography	31
Appendix	35
Abstract in Korean	37
Acknowledgements	39

List of Figures

Figure 1. Schematic description of the electrical double layer with corresponding potential distribution. The surface has a negative potential of ψ_s	3
Figure 2. Schematic description of ion concentration polarization with a corresponding concentration profile. N^+ refers the flux of cation and N^- refers the flux of anion.	4
Figure 3. Schematic view of salt counterion concentration profiles at different current densities. c_0 is the concentration of bulk electrolyte (reservoir).	7
Figure 4. A typical voltage-current curve with limiting and overlimiting regimes.	7
Figure 5. (a) Image of the assembled device. The inset shows its schematic view of essential components near the nanoporous junction. (b) Microscopic image of the device. Two microchannels with different L/A are connected by surface-patterned Nafion nanojunction. Main and buffer microchannels are depicted in red and blue, respectively.	12
Figure 6. $I-V$ responses of the devices with the microchannel cross-sectional area of (a) $3360 \text{ } \mu\text{m}^2$ (b) $1680 \text{ } \mu\text{m}^2$ and (c) $840 \text{ } \mu\text{m}^2$, respectively. In each graph, current value increases with L/A beyond the Ohmic regime. Comparing (a) to (b) and (b) to (c), larger cross-sectional area results in higher current. (d) Ohmic conductance increases proportional to A	16
Figure 7. OLC as a function of (a) depth or (b) L/A . In (a), data points are in a line with the theoretical prediction only when the z -directional length is larger enough than y -directional length (See the red circles and line). In (b), all data are well-agreed with the modified theoretical prediction as a function of $(L/A)^{-1}$, regardless of the z - and y -directional length.	17
Figure 8. Current rectifications came from the asymmetric L/A values of the forward and the reverse microchannel. Physical dimensions of the main and buffer microchannels are as depicted.	21
Figure 9. (a) Schematic illustration of the unit pattern of the microchannel array with an expected flow pattern on the anodic side (red). (b) Microscopic image of the device. Main and buffer microchannels are depicted in red and blue, respectively. In the main microchannel, $h_n = 13.5 \text{ } \mu\text{m}$ and $h_w = 31.5 \text{ } \mu\text{m}$	24
Figure 10. Visualization of recirculation flow at the anodic end of the microchannel	

array. The red and blue arrows indicate oleic acid droplets.....25

Figure 11. Microscopic images of before (top) and after (bottom) the 1000 minutes of operation under 5 V with (a) non-uniform and (b) uniform microchannel network. The boundaries of the networks are highlighted by the white broken line. The inset in (b) shows magnified view of the crystals formed inside the microchannel network.....27

Figure 12. Current-time responses from (a) non-uniform array under 5 V (b) uniform array under 5 V (c) non-uniform array under 10 V and (d) uniform array under 10 V.....27

List of Table

Table 1. Physical dimensions of all microchannels used in this work.....13

1. Introduction

1.1. Research Background

1.1.1. Electrical double layer (EDL)

Due to the fixed surface charge at the solid interface, an oppositely charged region of counterions develops in the liquid to maintain the electroneutrality of the solid-liquid interface [1]. For instance, if a solid surface is negatively charged, negative free ions in the electrolyte are expelled whereas positive free ions in the vicinity of the interface are attracted and form an electrical double layer (EDL). This screening region consists of bound or mobile charges which are in turn named as Stern layer and diffuse layer, respectively. In the scheme of Helmholtz plane, the Stern layer is defined as the layer between the inner and outer Helmholtz planes where specifically adsorbed cations reside. Here the potential and the charge distribution depend linearly on the distance from the surface. The complete picture can be further constructed following the Gouy-Chapman theory [2] as in Figure 1. In this figure, the surface is negatively charged therefore has a negative potential ψ_s . The potential at an imaginary plane separating the two layers is referred to as ζ potential. Assuming that the potential near the surface is relatively small, the distribution can be simplified as linearized Poisson-Boltzmann equation:

$$\nabla^2\psi = \frac{d^2\psi}{dz^2} = \kappa^2\psi(z) \quad (1)$$

with the Debye-Hückel parameter $\kappa = \left(\frac{F^2z^2c_0}{\varepsilon_0\varepsilon_rRT}\right)^{1/2}$.

Where ψ is the electric potential due to the surface charge, z is the distance from the surface, ε_0 is the permittivity of free space, ε_r is the relative permittivity of the electrolyte, R is the gas constant, T is absolute temperature, F is the Faraday constant, z is the valence of ionic species, and c_0 is the molar concentration. Since Equation (1) implies that the potential decays exponentially in the diffuse layer near a flat surface, the characteristic thickness of EDL, λ , can be defined as the inverse of the Debye-Hückel parameter:

$$\lambda = \kappa^{-1} = \left(\frac{\varepsilon_0\varepsilon_rRT}{F^2z^2c_0}\right)^{1/2} \quad (2)$$

For a 1 mM electrolyte where each ion is singly-charged and the ionic strength is

equal to the concentration, λ is ~ 10 nm at room temperature.

When the geometric scale of a certain fluidic system is comparable to its EDL thickness, the EDL can expand and entirely covers the channel interior. Therefore, the fluidic channel has a preference for a specific charge species. In case the surface is negatively charged, the charge selective nature operates on positive ions while negative ions are repelled by the electrostatic potential of the overlapped EDL. This imbalanced ion transportation may significantly impact the ion distribution on both sides facing the nanostructure, which leads us to the following section.

1.1.2. Ion concentration polarization (ICP)

Earlier experimental studies reported that fluidic channels of ~ 50 nm in thickness exhibit ion-selectivity (or perm-selectivity) due to the EDL overlapping [3, 4]. Assuming that a nanomembrane immersed in the electrolyte is composed of an array of cation-selective nanochannels and an external electric field is applied in the direction perpendicular to the nanomembrane, the ions in the bulk solution are provided the driving force to move in the direction normal to the membrane. Under such bias, only positive ions (cations) can penetrate through the membrane from anodic to cathodic side whereas negative ions (anions) cannot. As the cations escape from the anodic side, the anions should decrease its population to meet the electroneutrality, which in turn results in the ion-depleted zone at the anodic side of the membrane. Contrarily, anions are transported toward the cathodic side and build up an ion enrichment zone. The overall situation is schematically illustrated in Figure 2. This typical behavior under the electric field gradient is called ion concentration polarization (ICP). The concept of local ion removal has been widely applied for desalination strategies [5-8].

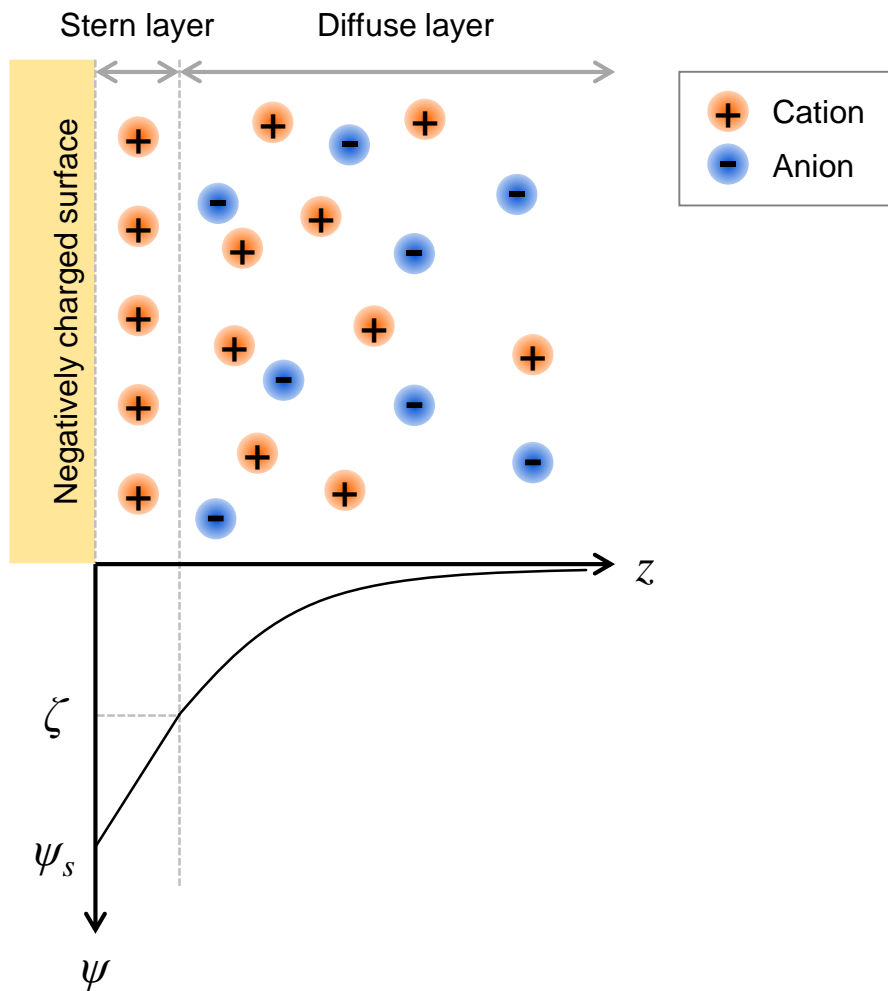


Figure 1. Schematic description of the electrical double layer with corresponding potential distribution. The surface has a negative potential of ψ_s .

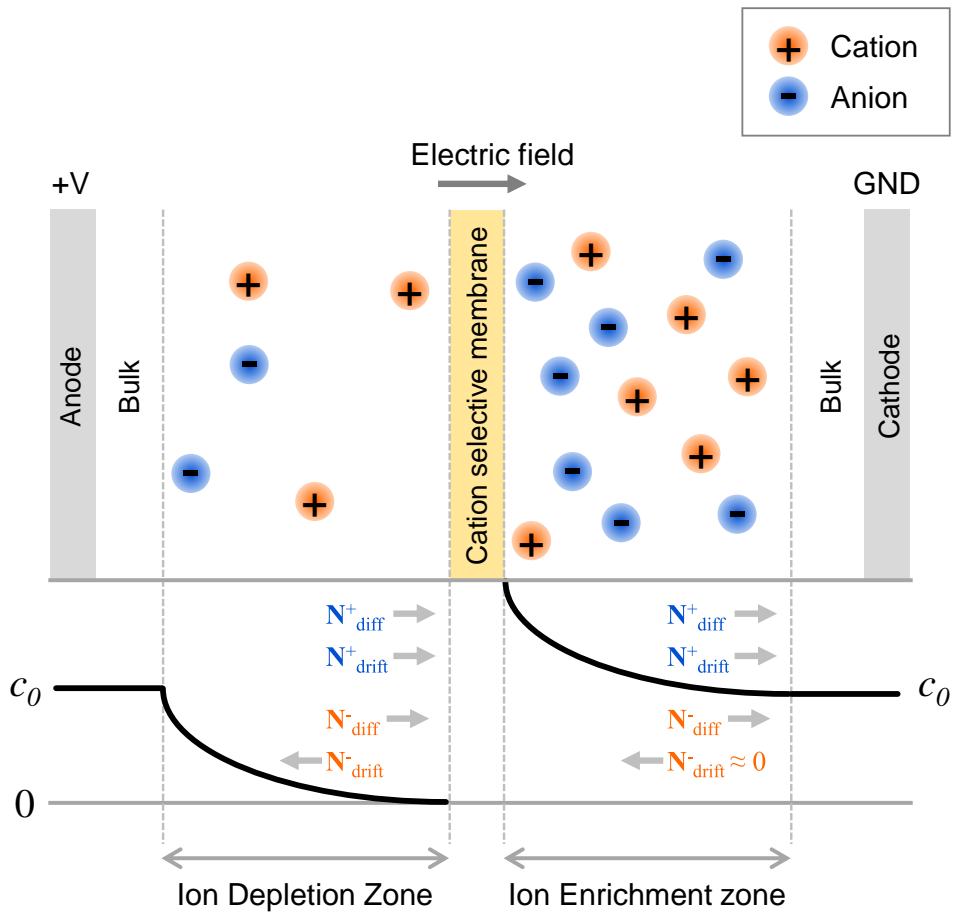


Figure 2. Schematic description of ion concentration polarization with a corresponding concentration profile. N^+ refers the flux of cation and N^- refers the flux of anion.

1.1.3. Limiting and overlimiting current

ICP may induce a significant ion concentration gradient near a charge-selective membrane thus affect the ion current flux. The ion transport and concentration are limited in the boundary region (diffusion layer) near the membrane surface, and the distance is assumed to be approximately 10-100 μm sitting between the bulk and the membrane [3]. Following the theories employing the local electroneutrality assumption, the interfacial electrolyte concentration in the depleting solution tends to be zero, and the potential drop through the diffusion boundary layer tends to be infinity when the current density approaches its limiting value [9]. Thus, the ionic flux is expected to be saturated and the corresponding current reaches the limiting current (I_{lim}). Under the assumption that each ion species are identical in terms of valence, diffusivity, and mobility, $I_{lim} = zFDc_0/L$ where z is the valence, F is the Faraday constant, D is the diffusivity of ion, c_0 is the bulk concentration, and L is the distance from the interface which is large enough to reach the bulk environment. The concentration profiles from the anodic side of the membrane to the bulk electrolyte is schematically described in Figure 3. It is shown that the concentration at the anodic interface of the membrane reaches zero when the current density is equal to I_{lim} at its steady state.

However, some effects coupled with the passage of intensive currents may prevent the saturation [9]. There have been attempts to provide a rationale for the fact that the current density surpasses the limiting one such as water splitting, gravitational convection, or thermoconvection. Among the interpretations presented in earlier papers, it has been widely accepted that the overlimiting current transfer originates from the reduction of the effective thickness of the diffusion boundary layer by a growing space charge region [10]. Rubinstein and Segel numerically and analytically exhibited an oscillatory instability at sufficiently high voltages and predicted that this instability can be a signal of further turbulent-like transitions. In the same year, Rubinstein and Shtilman showed that the bulk charge region near the membrane can further develop and this may lead to steady current much greater than the limiting one[11]. This is a logical consequence drawn from the physical insight that the local Debye radius can be much greater than that in the bulk as the concentration near the membrane approaches zero. Hence, the inflection could be explained when the

electroneutrality postulation in classical interpretation was replaced by the full Poisson equation. Later, Zaltman and Rubinstein introduced electroconvection, the flow which contains a significant amount of charge carriers of both signs, as a main source of overlimiting current [12]. As the interface concentration decreases, the non-equilibrium structure of EDL advances which leads to conductance instability. As a result, a macroscopic vortical electroconvective flow develops which destroys the diffusion layer at the solid/liquid interface [13]. This analysis plays a key role in explaining the enhanced ionic mass transport in the overlimiting regime. Figure 4 illustrates a typical voltage-current curve when the above-mentioned factors are considered. It is shown in the curve that the limiting current plateau is followed by an upward climb as the voltage is raised.

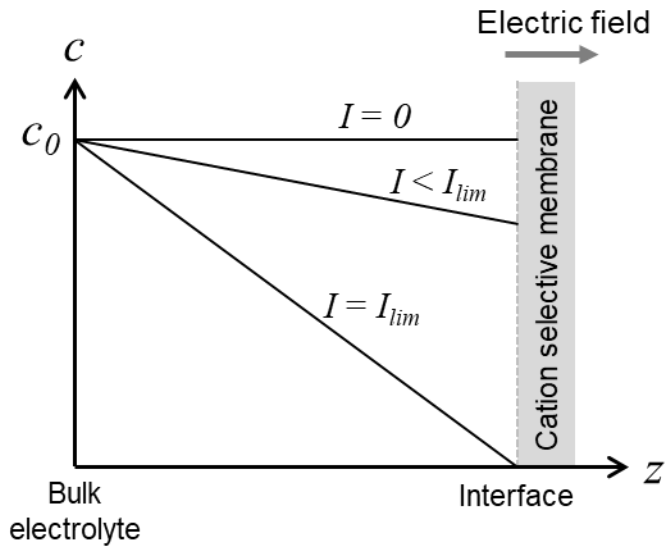


Figure 3. Schematic view of salt counterion concentration profiles at different current densities. c_0 is the concentration of bulk electrolyte (reservoir).

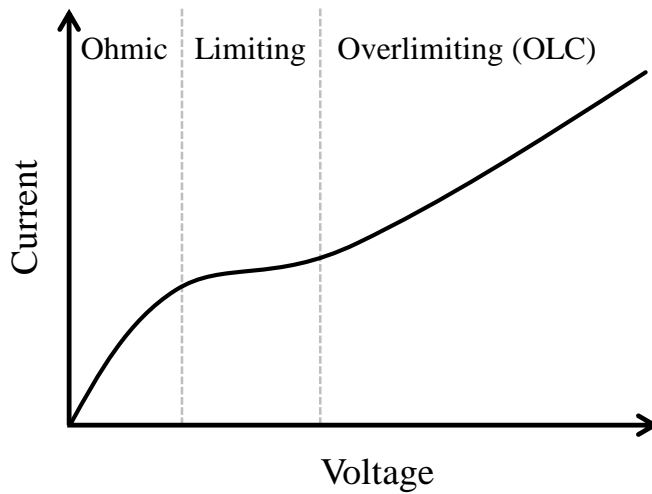


Figure 4. A typical voltage-current curve with limiting and overlimiting regimes.

1.2. Motivation and purpose of the research

As a natural extension of microfluidics and nanotechnology, nanofluidics has attracted much attention and imagination from many researchers for the past several decades [14, 15]. A large amount of research work has been focused on the physics of ion-selective transport in nanoscale and ICP phenomena which have enabled extensive applications on environmental engineering and diagnostics. The mathematical models have been an important plank to understand the geometrical effects of charged sidewalls from the basics [16], however, convergence was not necessarily found in practical cases which urges to re-consider the established idea. In this context, the thesis proposes an expansion of the theoretical approach to surface-driven ion transport mechanism beyond its dimensional limitation. Microchannels covering a wide range of geometric variety were constructed and the strength of ionic conductance was quantitatively analyzed. A geometrical parameter was invented as a result to bridge the theoretical model and a practical system. The parameter is then employed to build a fluidic diode which overcomes the limitations of previously reported devices [17-19]. Compared to those who based on the nanoscale asymmetry, its current rectification property holds even in relatively high levels of ion, and the fabrication labor is much reduced. Further, the scope of the research is broadened into a network of surface conductive microchannels. An application strategy to reduce channel clogging in microchannels is presented which has been a bottleneck of stable long-term operation of the devices. It demonstrates a fluidic system with a precisely controllable flow pattern and its necessity was emphasized by the operation with enhanced stability over time compared to its counterpart with conventional uniform design. It was shown that a non-uniform fluidic system may enhance the internal flow in the microchannels, thereby reducing the chance of local concentration or crystallization happening. Within this scheme, the current stability stems entirely from the geometrical configuration of the microchannels, therefore it can function without any external control or energy input.

1.3. Outline of dissertation

Each part of the manuscript is presented in the following order. The first chapter presents a summary of the basic mechanisms and previous research works which form the basis of this study. The main part consists of two distinct topics, each of which can be found in chapters 2 and 3. The objective of chapter 2 is to generalize the present 2-dimensional current flux analysis into the 3-dimensional case. A single geometric factor was then extracted to explain the discrepancy found from conventional approaches. Then in the subsequent chapter, a fluidic system where more than one microchannels compose a network was studied in this surface-driven transport regime. A general conclusion is given in the last chapter with perspectives for future work.

2. Surface conduction in a microchannel

2.1. Introduction

Being represented by the Nernst-Planck equation, the classical theory to elucidate ion transportations through aqueous solution includes the contribution of diffusion, drift, and convection [1, 2, 20]. While numerous experimental and theoretical studies have been conducted using the equation so far, recent findings that have been accelerated by the advances of micro/nanofluidic research teach us that there are additional significant mechanisms beyond the equation [13, 16, 21-28]; electroosmotic instability (EOI), electroosmotic flow (EOF), surface conduction (SC) and diffusioosmosis. Among them, the electrokinetic operation at SC regime affords versatile utilities in micro/nanofluidic platforms especially due to its stability [13, 29-33]. Such platforms with extremely high surface to volume ratio allow the surface effect to predominate over the volume (or bulk) conduction which has been mainly considered in the classical Nernst-Planck equation. SC is defined as the flow of excess charges in an electrical double layer (EDL) formed near a charged surface [16]. There are two major factors that determine the regime of ionic current; (i) the characteristic length scale and (ii) the surface charge density of the substrate. Smaller length and higher surface charge density drive the system to surface effect-dominant regime, *i.e.* SC regime. While seminal theoretical characterization of SC has been widely applied for stable electrokinetic operations or enhancing system conductance [23, 30, 34-37], the analysis has been usually carried based on two-dimensional approximation which inevitably requires at least one infinitely long axis, unless it was conducted using a direct numerical simulation [38]. When a system has a confined geometry such as practical micro/nanofluidic devices, the third axis, which has been neglected in two-dimensional approximation, should be considered.

In this work, therefore, we experimentally investigated the three-dimensional geometric effect on SC by employing a micro/nanofluidic platform that consists of two microchannels connected with Nafion nanojunction. The aspect ratios of the microchannel cross-section were designed to be varied from 0.003 to 1 so that the conductance was measured from an approximated two-dimensional limit to a three-dimensional geometry. As a function of only microchannel depth, the measured conductance values were out of theoretically predicted range, especially when the

aspect ratio approaches to 1. Alternatively, the third dimensionality was included in the calculation of a volume density of fixed charges so that the perimeter to area ratio of microchannel cross-section was extracted as a single parameter to fit all of the conductance data. The parameter would be utilized as a significant design rule for various micro/nanofluidic devices such as power-efficient desalination device, highly sensitive electrical (bio-)sensors, diagnostics tools or ionic circuit components.

2.2. Experimental details

2.2.1. Device fabrication and materials

The microchannels were molded by the general PDMS fabrication process [39]. Briefly, PDMS solution at the ratios of pre-polymer (PDMS, Sylgard 184, Dow corning) to curing agent of 10:1 was mixed and degassed for an hour. After pouring on lithographically constructed Si wafer, it was cured at 75°C for 4 hours. The demolded PDMS block and Nafion (Sigma Aldrich, USA)-patterned glass substrate were irreversibly adhered by O₂ plasma treatment (Cute-MP, FemtoScience, Korea). The Nafion was patterned by surface patterned method [40, 41]. Both microchannels were filled with 1 mM KCl solution.

2.2.2. Experimental setups

Ag/AgCl electrodes were inserted at both reservoirs to apply external voltage (SMU238, Keithley, USA). The voltage was swept from 0 V to 4 V at 0.2 V/30 sec for I-V measurement and 0 V to 4 V, 4 V to -4 V and -4 V to 0 V at ± 0.2 V/30 sec for current rectification measurement. Current value at each voltage step was obtained by the customized Labview program.

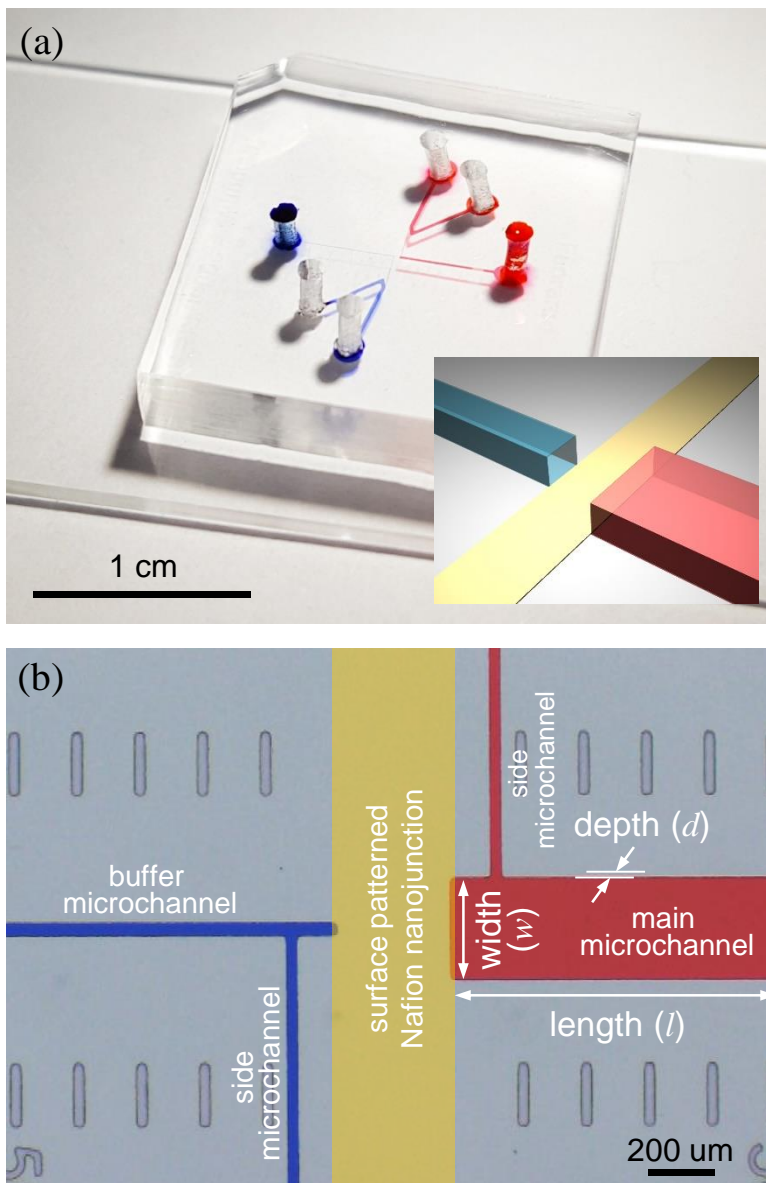


Figure 5. (a) Image of the assembled device. The inset shows its schematic view of essential components near the nanoporous junction. (b) Microscopic image of the device. Two microchannels with different L/A are connected by surface-patterned Nafion nanojunction. Main and buffer microchannels are depicted in red and blue, respectively.

Table 1. Physical dimensions of all microchannels used in this work.

d [μm]	w [μm]	A [μm^2] $=dw$	L [μm] $=2(d + w)$	L/A [μm^{-1}]
3	70	210	146	0.70
5	42		94	0.45
7	30		72	0.34
10.5	20		61	0.29
15	14		58	0.28
3	140	420	286	0.68
5	84		178	0.42
7	60		132	0.31
10.5	40		101	0.24
15	28		86	0.20
3	280	840	566	0.67
5	168		346	0.41
7	120		252	0.30
10.5	80		181	0.22
15	56		142	0.17
3	560	1680	1126	0.67
5	336		682	0.41
7	240		492	0.29
10.5	160		341	0.20
15	112		254	0.15
3	1120	3360	2246	0.67
5	672		1354	0.40
7	480		972	0.29
10.5	320		661	0.20
15	224		478	0.14

2.3. Results and discussion

2.3.1. Experimental Designs

The device we employed in this work is shown in Figure 5(a). PDMS-glass bonded micro/nanofluidics devices were fabricated using standard soft-lithography [39] for microchannels and surface patterning for Nafion nanojunction [42]. Figure 5(b) gives a magnified view near the nanojunction. Two microchannels (main (red) and buffer (blue)) were connected by patterned Nafion bridge. Air-valves were installed at the side microchannels for the easiness of experimental labors. In order to eliminate disturbances from uncontrolled hydraulic pressure, high Laplace pressure formed at liquid/air interface inside the side microchannels was utilized as a virtual valve, allowing to obtain the identical electrokinetic responses with a 1-dimensional micro-nano-microchannel device [43]. Such practical devices inevitably possess a three-dimensional constriction as shown in the inset of Figure 5(a), imposing a critical limitation on two-dimensional analysis. In order to explore their electrokinetic properties, one of geometrical factors should be kept in constant and, in this work, the cross-sectional area ($A = dw$) of the main microchannel was designed to keep the Ohmic conductance (or bulk conductance) (σ_{Ohm}) constant in each design. The design parameters (width (w) and depth (d)) of main microchannel were listed in the first and the second column of Table 1. While A remained constant, the perimeter ($L = 2(d+w)$) of the main microchannel was varied accordingly. Consequently, in that aspect, one would be able to obtain a variation of L/A , perimeter to cross-sectional area ratio. It is the parameter of interest in this study in that it represents the variation of L at constant A , *i.e.* the surface conduction effect without the consideration of the Ohmic conduction. Five sets of devices whose A 's were doubled from the previous set were fabricated for further investigation over the wide range of L/A .

2.3.2. Ohmic-limiting-overlimiting current measurements

The current-voltage relations of all dimensions listed in Table 1 are plotted in Figure 6(a)-6(c). Additional data sets are presented in the Appendix. The voltage was swept at 0.2 V/30 sec from 0-4 V. As expected, the slopes in the voltage range of 0-0.6 V

(σ_{Ohm}) were almost overlapped because A was constant in each plot in Figure 6(a). The same scenario was applied to Figure 6(b) and Figure 6(c) as well. Statistical analysis showed that σ_{Ohm} was roughly proportional to A as shown in Figure 6(d). More importantly, the overlimiting conductance (σ_{OLC}) was significantly altered depending on d in each plot in Figure 6(a)-6(c). σ_{OLC} is the fingerprint of electrokinetic property within micro/nanofluidic devices or nanoporous membrane system, describing additional current increment followed by the Ohmic regime and limiting current regime [3, 11, 23, 35, 44-47]. It can be extracted by reading the slope of $I-V$ curve at a larger voltage substantially away from the Ohmic regime. The remarkable observation is that higher L/A resulted in higher σ_{OLC} even under the same A . This means that one has to fully assess the three-dimensional structure (w , d , and l) to utilize a quantitative (or predictable) $I-V$ relation in micro/nanofluidic device for own purposes.

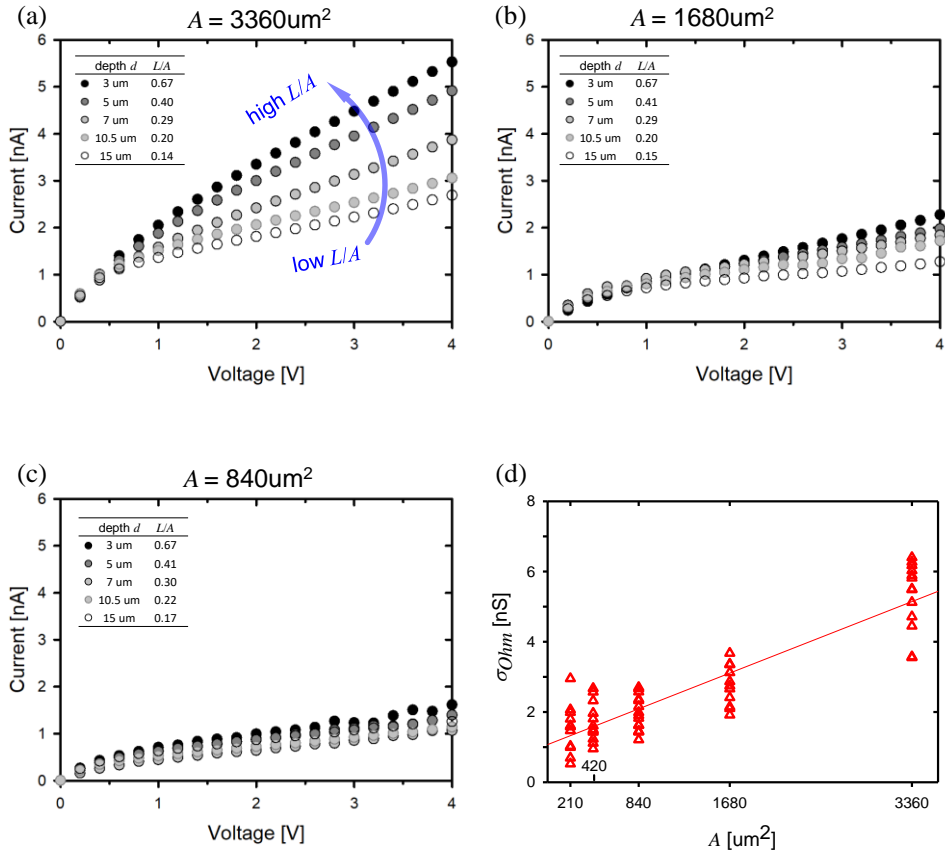


Figure 6. I - V responses of the devices with the microchannel cross-sectional area of (a) $3360 \mu\text{m}^2$ (b) $1680 \mu\text{m}^2$ and (c) $840 \mu\text{m}^2$, respectively. In each graph, current value increases with L/A beyond the Ohmic regime. Comparing (a) to (b) and (b) to (c), larger cross-sectional area results in higher current. (d) Ohmic conductance increases proportional to A .

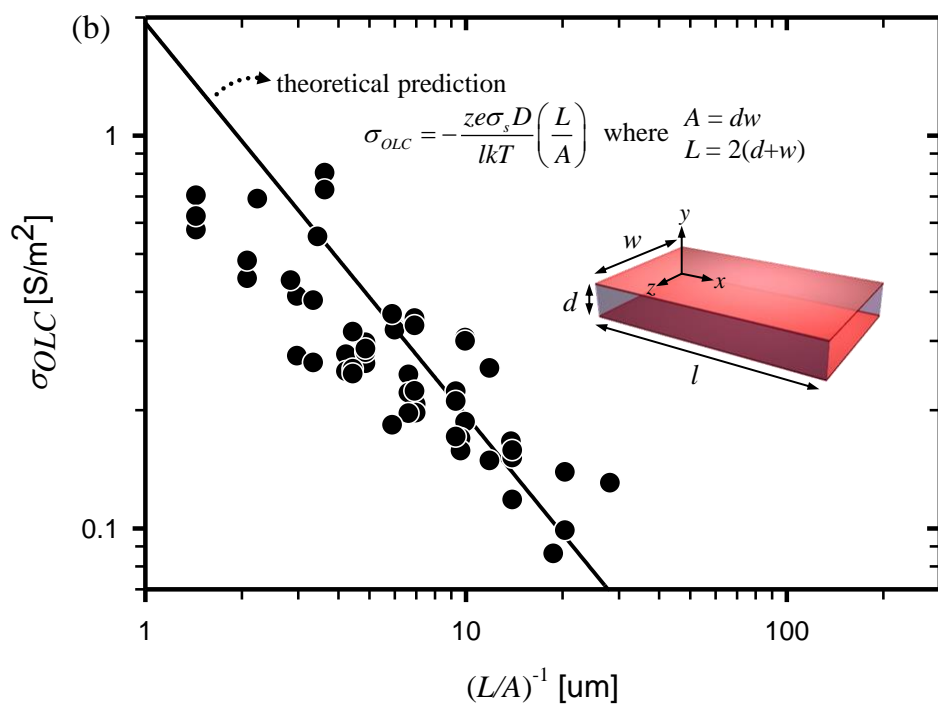
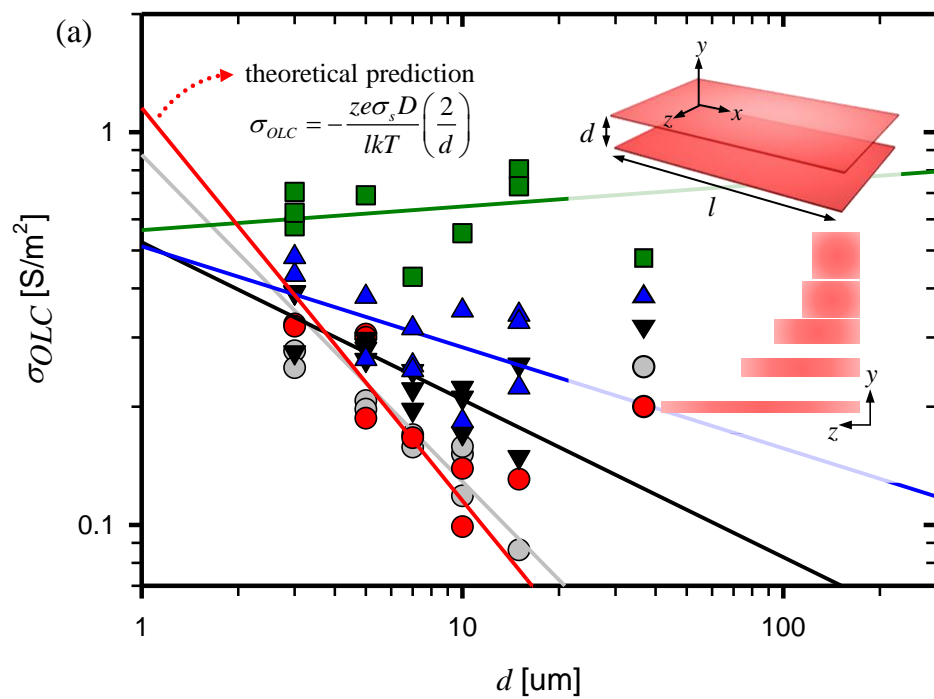


Figure 7. OLC as a function of (a) depth or (b) L/A . In (a), data points are in a line with the theoretical prediction only when the z -directional length is larger enough than y -directional length (See the red circles and line). In (b), all data are well-agreed with the modified theoretical prediction as a function of $(L/A)^{-1}$, regardless of the z - and y -directional length.

2.3.3. 2D analysis vs 3D analysis

In order to investigate the effect of dimensionality on σ_{OLC} , both previously reported two-dimensional analysis and our three-dimensional analysis were conducted and the comparison results were shown in Figure 7(a) and Figure 7(b), respectively. In Figure 7(b), σ_{Ohm} had to be tailored in advance to sort out its influence on σ_{OLC} . In other words, cross-sectional areas of all main microchannels were converted into a single value, 210 um^2 for convenience, maintaining the ratio between w and d . The schematics of dimensionality are depicted in the insets of each plot. The conventional two-dimensional relation [16, 22, 23], $\sigma_{OLC} = -\frac{zeD}{lkT} \left(\frac{2\sigma_s}{d} \right)$ was held in the case of extremely thin microchannel whose z -directional length could be considered as an infinity compared to the y -directional length (see red circles and line in Figure 7(a)). In this equation, σ_s , z , e , D , k and T are the surface charge of material, valence of ion, elementary charge, diffusion coefficient, Boltzmann constant and absolute temperature, respectively. σ_s/d represents a surface charge contribution of a charged wall at distance d . The value of l was selected as $O(1)$ mm. However, the exponent of d deviated from -1 as the shape of microchannel cross-section became a square whose z -directional length is now comparable to the y -directional length. Therefore, the full understanding of three-dimensional constriction should be required to setup the appropriate design strategy of an efficient micro/nanofluidic device or nanoporous membrane system whose electrical performance is predominantly determined by σ_{OLC} . [7, 41, 47] Here we considered the third-dimensional constriction along z -axis as shown in the inset of Figure 7(b). Starting from the Nernst-Planck equation in a negatively-charged long microchannel (d and $w \ll l$) with thin EDL approximation ($\lambda_D \ll d$ and w , where λ_D is the Debye screening length), the excess charge is expressed as ρ_v/e where ρ_v is the volume density of fixed charge, *i.e.* the number of fixed charges inside a unit volume enclosed by charged surfaces. While the two-dimensional analysis employed ρ_v as $\frac{\sigma_s}{ze c_0 d}$ where c_0 the reservoir concentration [16], here the three-dimensional constriction provided ρ_v as $\frac{\sigma_s}{ze c_0} \left(\frac{2}{d} + \frac{2}{w} \right)$ which included the surface charged effects from all enclosed walls under the assumption that the edge effect at the corners of microchannel was negligible. Since the ionic flux (j) is proportional to $\rho_v V$ in the SC regime, σ_{OLC} (=

j/V) should be $-\frac{ze\sigma_s D}{kT} \left(\frac{2}{d} + \frac{2}{w} \right)$ where the last multiplier, $\frac{2(d+w)}{dw}$, corresponds to the L/A in this work. Note that this three-dimensional equation is also applicable in two-dimensional analysis as w approaches infinity.

All data points from Figure 7(a) were rearranged as a function of $(L/A)^{-1}$ as shown in Figure 7(b). The data was well-agreed with the theoretical prediction so that we can conclude that L/A is the unified parameter that governs OLC in a microchannel where SC is major current transportation mechanism. (Note that electroosmosis also minorly contributed to the current transportation, especially when the characteristic length scale of microchannel was over 10 μm so that the data in Figure 7(c) were slightly deviated from theoretical prediction.) It implied that the combination of various L and A would convey an adjustable conductance so that this analysis would play a deterministic role for designing a micro/nanofluidic device or a membrane system. For example, the compartmentalization of macrochannel (*i.e.* increase L with fixed A) would provide superior conductance and stability for realizing a high-throughput massive parallel micro/nanofluidic devices [24, 29, 35, 36]. It is also feasible to provide a concrete theoretical support whether a thin, but wide channel would have stable or unstable electroconvection, while the electroconvection is stabilized very quickly within the channels (or pores) confined in both directions (*i.e.* the width and height both being finite)[45]. In the fundamental aspect, the parameter would strengthen the previous literatures that utilized a perimeter to cross section area as the parameter to define nanopore size [48-51]. In the meantime, one can manipulate the ionic current in a stretchable or deformable micro/nanofluidics [52-54] (*i.e.* increase A with fixed L or adjust both A and L , respectively) at one's discretion for developing efficient electrical sensors [55] or diagnostics tools [56-58].

2.4. Application for nanofluidic diode

For the simplest practical demonstration, two microchannels of different L (*i.e.* different SC) with constant A (*i.e.* constant σ_{ohm}) were connected by Nafion nanojunction for realizing a micro/nanofluidic diode [18, 19, 34, 59-61] by our strategy. We choose the microchannel dimensions as in the schematics of Figure 8(a)

and Figure 8(b) and successfully obtained the rectification factor of 1.95 and 6.02, respectively. According to our analysis, a single parameter, L/A , would strategically manipulate the rectification factor of nanofluidic diodes.

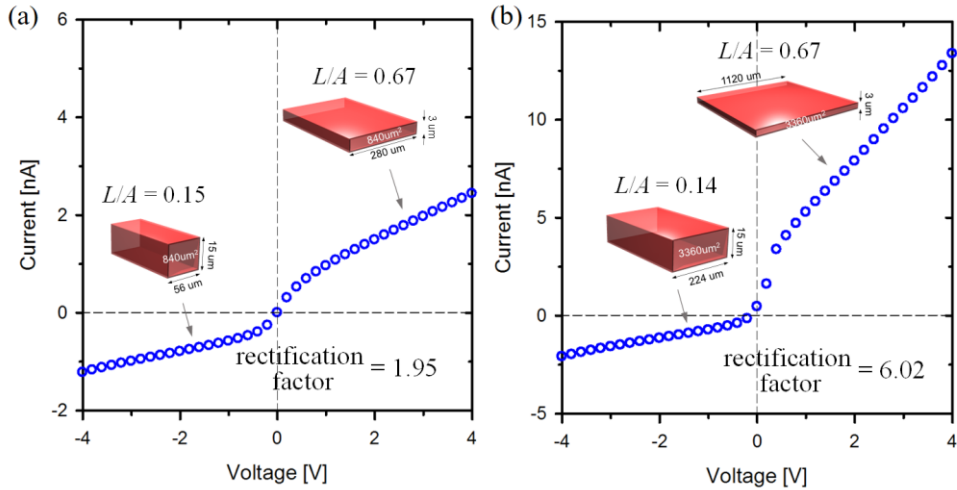


Figure 8. Current rectifications came from the asymmetric L/A values of the forward and the reverse microchannel. Physical dimensions of the main and buffer microchannels are as depicted.

2.5. Conclusions

In conclusion, since a two-dimensional analysis has inherent limitations from the assumption of an infinite axis, here we present a rigorous three-dimensional analysis of surface conductive ion transportation through a microchannel. By employing a micro/nanofluidic device that had various geometrical variations, the unified parameter of $L/A = 2(d+w)/dw$ was extracted and it successfully fits all of OLC data which had been largely deviated from the two-dimensional analysis. Lastly, a simple micro/nanofluidic diode was demonstrated by proper choices of L/A . The strategy would rejuvenate the robustness of surface conductive ion transportation mechanism in a practical micro/nanofluidic device or nanoporous membrane system.

3. Prevention of undesirable crystallization in non-uniform microchannel networks

3.1. Introduction

In many flow-based processes crystals and particles, either coming from a chemical reaction or a flowing suspension can be produced and deposited within the processing equipment [62]. This is often undesirable and may cause serious operational problems since it reduces the productivity and effectiveness of the electromembrane performance as well as increasing maintenance costs. Either the mechanism is reversible or irreversible, the channel compartments should go through cleaning or be replaced if the accumulation is unwanted and this strictly restricts their performance and widespread application. Many promising strategies including surface modification, feed water pretreatment, monitoring, and regular cleaning have been suggested from the lab-scale investigations to full-scale plants to understand the accumulation mechanism and to mitigate the negative impacts. [63-70] Nevertheless, these additional processes are often sensitive to the chemical composition of scale-forming factors which restricts its applicability and they inevitably increase the complexity of the production line as well as consume electrical energy which eventually increases the operational expenses.⁴⁵ In this work, therefore, we apply the recirculating flow as a passive, i.e. without external energy input, anti-crystallization design using the geometrical non-uniformity regardless of crystallizable species.

3.2. Experimental details

3.2.1. Device fabrication and materials

The microchannels were molded by the conventional fabrication process as described in the previous chapter [39]. The polydimethyl-siloxane (PDMS, Sylgard 184, Dow corning) blocks where microchannel arrays were engraved were irreversibly bond to Nafion (Sigma Aldrich, USA)-patterned glass substrate by O₂ plasma treatment (Cute-MP, FemtoScience, Korea). The Nafion was patterned by the surface patterned method [40, 41]. For the visualization of recirculating flow, the mixture of 1 mM KCl and ultrasonicated Oleic acid droplets (Canola oil, Wesson,

USA) was injected to both microchannels. The microchannel network was filled with calcium chloride (CaCl_2) solution of 10 mM for the crystallization demonstration.

3.2.2. Microchannel designs

Each channel compartment is 1 mm in width, 6 mm in length, and 15 μm in depth and consists of 23 microchannels which were separated by micro-fin structures between them. The micro-fin structures are 22.5 μm in width, 2.5 mm in length, and 15 μm in depth. The spacing (h_w or h_n in Figure 9(a)) between the micro-fins became the microchannels where electrolyte was filled in. The devices were categorized into two types: uniform and non-uniform. In uniform devices, all the microchannels were identical, that is, $h_w = h_n$. On the other hand, the spacing was altered to be $h_w = 31.5$ μm and $h_n = 13.5$ μm in non-uniform devices so that h_w is approximately 2.33 larger than h_n . The cross-sectional area (A) and perimeter (l) of the microchannel surface area were kept the same in both cases, therefore the surface and bulk conduction were identical. Figure 9(b) shows the microscopic image of a non-uniform device. In the figure, the microchannels were filled with red (main channel) or blue (buffer channel) ink for demonstration.

3.2.3. Experimental setups

Ag/AgCl electrodes were inserted at both reservoirs to apply external DC voltage (SMU238, Keithley, USA). The voltage value was carefully chosen to let the system operate in overlimiting regime. Current values were measured by a customized Labview program at each voltage step. The buffer microchannel was always electrically grounded.

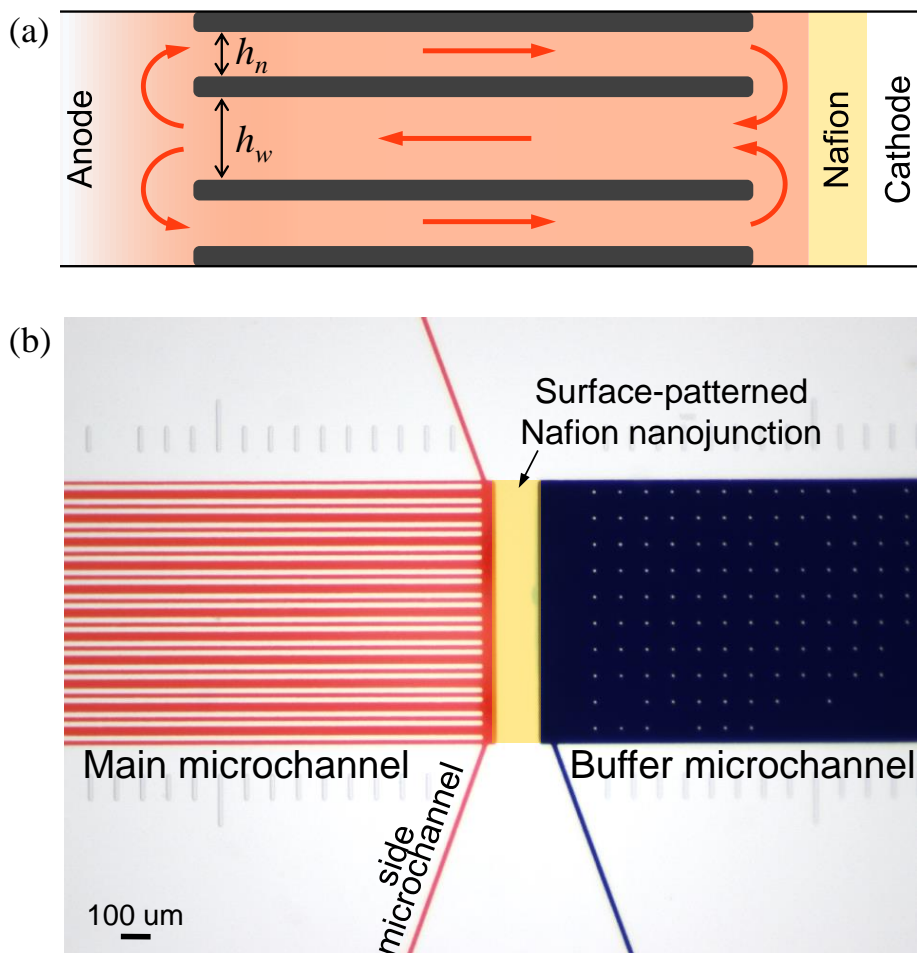


Figure 9. (a) Schematic illustration of the unit pattern of the microchannel array with an expected flow pattern on the anodic side (red). (b) Microscopic image of the device. Main and buffer microchannels are depicted in red and blue, respectively. In the main microchannel, $h_n = 13.5 \text{ } \mu\text{m}$ and $h_w = 31.5 \text{ } \mu\text{m}$.

3.3. Results and discussion

3.3.1. Visualization of recirculation flow

The first part of the experiment is dedicated to the visualization of the recirculation flow in the non-uniform structure designed in this work. Oleic acid droplets were added into the 1 mM KCl electrolyte as a flow tracer. The series of micrographs in Figure 10 were taken every 8 seconds at the end of the micro-fin structure when 5 V was applied across the microchannels. Two of the oil droplets were highlighted by the blue and red arrows for tracking and this shows that they changed the direction to re-enter the smaller microchannel as they reach the end of the larger microchannel. A similar trend was observed from other droplets therefore one can reasonably assume that this trend reflects the recirculating fluidic flow inside the array structure.

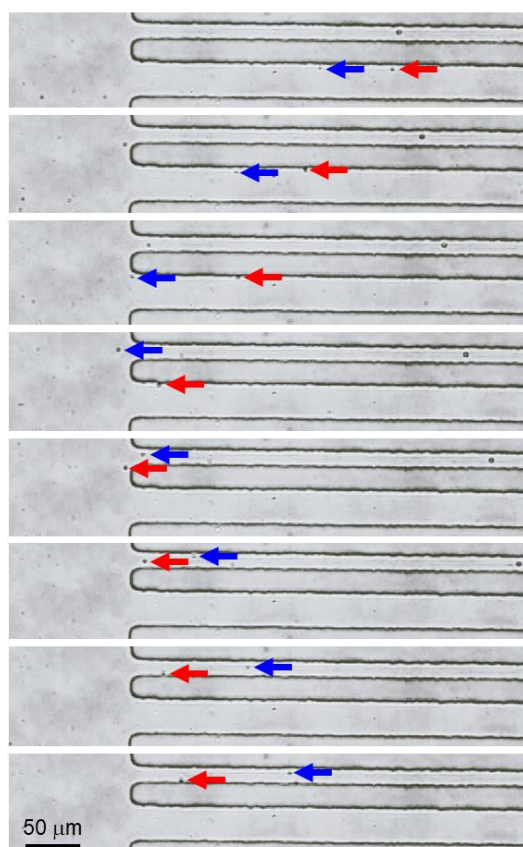


Figure 10. Visualization of recirculation flow at the anodic end of the microchannel array. The red and blue arrows indicate oleic acid droplets.

3.3.2. Current responses and microscopic observation

As a crystallizable ionic species, the microchannel network was filled with calcium chloride (CaCl_2) solution under the consideration that it is one of the most common sources of precipitation scaling. [63, 71] Its concentration, 10 mM, is supposed to be representative of natural seawater condition. The calcium ions ambient in the electrolyte may form calcium hydroxide ($\text{Ca}(\text{OH})_2$) which is an inorganic compound and slightly soluble in water (solubility ~ 23 mM at 20°C).

In the microscopic images shown in Figure 11(a) and 11(b), it is remarkable that solid-phase $\text{Ca}(\text{OH})_2$ crystals were formed on the microchannel surface only in the uniform channel network which has been rarely observed from their counterparts. These crystals were observable after one-hour operation and, eventually, several microchannels in the uniform network are completely blocked by the crystals as shown in the inset of Figure 11(b). Their spatial distribution has not shown any specific pattern as anticipated from the random formation of the vortex behind the micro-fins. This emphasizes that the crystal formation in uniform arrays can severely impact the liquid flowing thereby the current passage as well. As shown in Figure 12, current-time responses from each type of device were measured after an external voltage of 5 V or 10 V was applied as a step function at $t = 0$. The current was measured every 1 minute for 1000 consecutive minutes. The voltage was carefully chosen to let the system operate in an overlimiting regime. All devices experienced ~ 30 minutes of membrane stabilization followed by the steady OLC state. In the steady-state, the deviation from the stable current of ~ 42 nA was indistinctive in non-uniform cases as in Figure 12(a). On the other hand, current fluctuation appeared in the uniform network device, which indicates that the device may have undergone a substantial change in its current flow pattern. The fluctuation is less than 43% of its steady-state current of ~ 36 nA. It was also reaffirmed that the OLC is higher in a non-uniform network than the uniform cases.

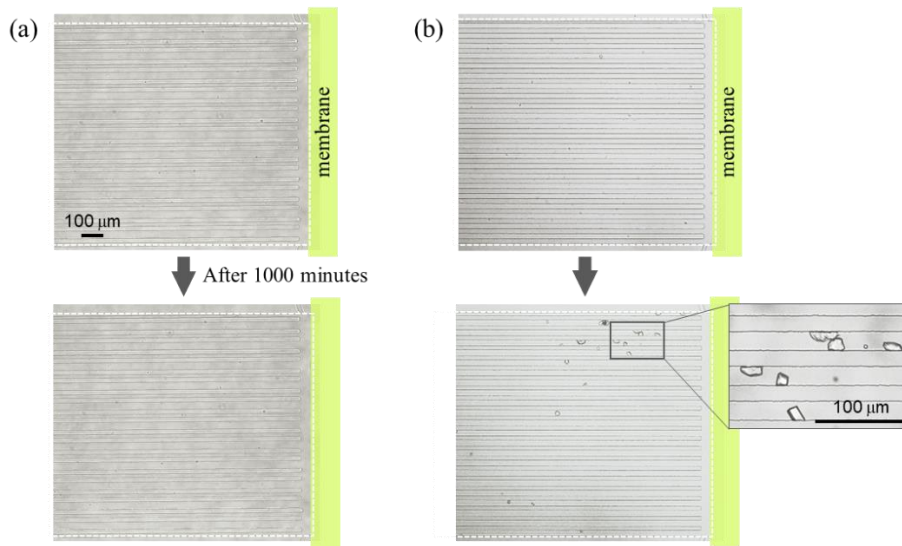


Figure 11. Microscopic images of before (top) and after (bottom) the 1000 minutes of operation under 5 V with (a) non-uniform and (b) uniform microchannel network. The boundaries of the networks are highlighted by the white broken line. The inset in (b) shows magnified view of the crystals formed inside the microchannel network.

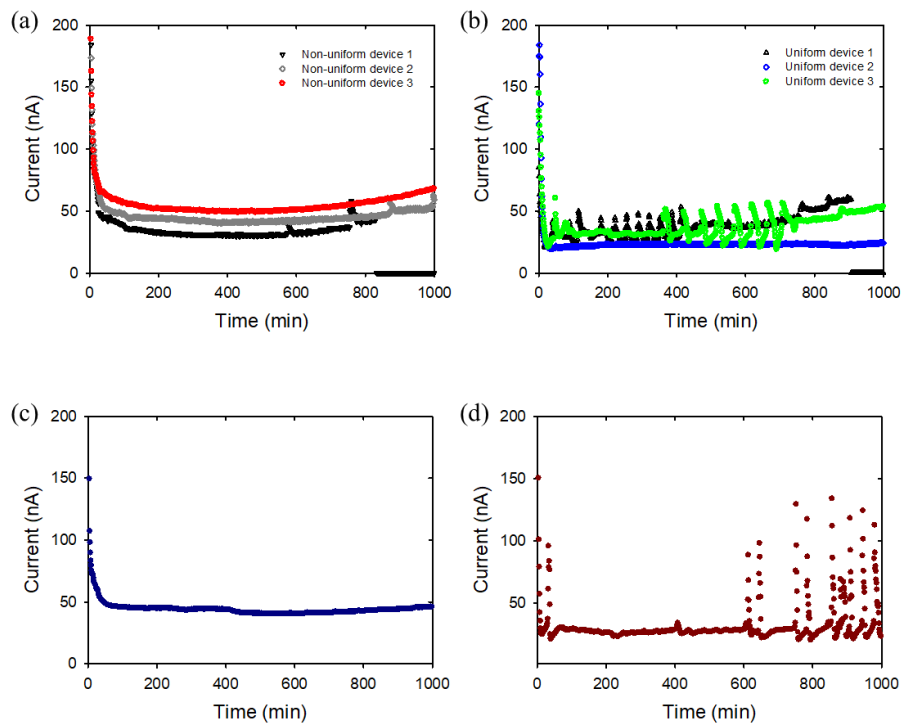


Figure 12. Current-time responses from (a) non-uniform array under 5 V (b) uniform array under 5 V (c) non-uniform array under 10 V and (d) uniform array under 10 V.

3.3.3. Discussion

Earlier studies have given ample evidence that water splitting may occur in an ion exchange membrane at overlimiting currents though the contribution of additional carriers (H^+ and OH^- ions) to the current flux is negligible [9, 72, 73]. If the OH^- ions generated near the interface in the course of water splitting meet the Ca^{2+} ions ambient in the electrolyte, the following reaction is favorable: $Ca^{2+} + 2OH^- \rightarrow Ca(OH)_2$ which produces calcium hydroxide ($Ca(OH)_2$) as a solid if the concentration of the compound exceeds its solubility. $Ca(OH)_2$ is relatively insoluble in water (1.73 g/L at 20 °C). Its dissolution in water is an exothermic process therefore its solubility is in inverse proportion to the temperature. Hence, the heat produced during the ICP further increases the possibility of precipitation and with its retrograde solubility, it becomes even harder to remove the crystals once they are formed in microchannels.

Prevention is thus an adequate strategy than the removal to minimize the channel failure and non-uniform geometry can effectively prevent the growth of $Ca(OH)_2$. When microchannels form a network, the OLC of the system depends on its geometrical configuration. Both experimental and theoretical current-voltage relations have demonstrated that OLCs increase with increasing non-uniformity and the visualization of internal recirculating flows indicates that the non-uniform arrays induce flow loops across the network enhancing the advective transport [74]. The enhanced flow within the microchannels can suppress both the nucleation and growth by minimizing local ion accumulation and, thus, the nuclei have less probability to be formed or fed and remain under observable size. Therefore, the increased mass transfer can reduce the crystal clogging of the network, so there was no presence of current fluctuation in non-uniform arrays. This anti-crystallization and the associated current stabilization are entirely passive processes that require no energy input.

3.4. Conclusions

In this work, we showed that the operation of an electrochemical membrane system gained stability when a geometrical variation was installed in their sequence. The crystal formation inside each microchannel was effectively suppressed by the enhanced recirculation flow, therefore the microchannel clogging was avoided in non-uniform arrays compared to their uniform counterpart. The crystal clogging process was determined by feed water composition, so the stabilization effect was examined in the case of CaCl_2 10 mM solution. The analysis showed that the overall current profile at constant voltage gained stability within ~ 1000 minutes of operation in the OLC regime. The proposed strategy is expected to have wide applicability to all kinds of feed water that may cause crystallization or precipitation. Thus this result can advance not only the fundamental understanding of nanoelectrokinetics but also the design rule of engineering applications of the electrochemical membrane.

4. Concluding remarks

A micro/nanofluidic platform was successfully fabricated by PDMS and Nafion perm-selective nanoporous membrane to investigate the OLC behavior in the surface conduction-dominant regime. In this platform, the ionic current tightly coupled with the fluidic flux depends on its geometric parameters, which implies that the operation properties can be modified with ease by altering the size and/or the sequence of each component. In the first section, the parameter (the ratio between the cross-sectional area and the perimeter of microchannel) was suggested as a connecting link that can expand the conventional 2-dimensional works into practical 3-dimensional microchannels. It was borne out at the same time that the SC is a major contribution to OLC when the channel size is under ~ 10 μm . With more than one microchannel in the platform, the effect of their arrangement on OLC was pronounced in the second section of the thesis. A series of parallel microchannels showed a stable current profile over time when non-uniformity is imposed in their sequence. It was confirmed that the geometrical varieties can induce additional flow patterns between the microchannels which has not been predicted in uniform arrays. The chance of crystallization from the electrolyte diminished as this recirculation flow stirs the fluid, therefore the channel clogging was passively avoided. This mechanism is expected to be further developed for a stable long-term operation of a micro/nanofluidic platform without the need for external energy input.

Bibliography

1. Schoch, R.B., J.Y. Han, and P. Renaud, *Transport phenomena in nanofluidics*. Reviews of Modern Physics, 2008. **80**(3): p. 839-883.
2. Probst, R.F., *Physicochemical hydrodynamics : an introduction*. 2nd ed. 1994, New York: John Wiley & Sons. xv, 400 p.
3. Kim, S.J., et al., *Concentration polarization and nonlinear electrokinetic flow near a nanofluidic channel*. Physical Review Letters, 2007. **99**(4).
4. Stein, D., M. Kruthof, and C. Dekker, *Surface-charge-governed ion transport in nanofluidic channels*. Physical Review Letters, 2004. **93**(3).
5. Jeon, S.I., et al., *Desalination via a new membrane capacitive deionization process utilizing flow-electrodes*. Energy & Environmental Science, 2013. **6**(5): p. 1471-1475.
6. Lee, J., et al., *Hybrid capacitive deionization to enhance the desalination performance of capacitive techniques*. Energy & Environmental Science, 2014. **7**(11): p. 3683-3689.
7. Kim, S.J., et al., *Direct seawater desalination by ion concentration polarization*. Nature Nanotechnology, 2010. **5**(4): p. 297-301.
8. Knust, K.N., et al., *Electrochemically Mediated Seawater Desalination*. Angewandte Chemie-International Edition, 2013. **52**(31): p. 8107-8110.
9. Urtenov, M.A.K., et al., *Decoupling of the Nernst-Planck and Poisson equations. Application to a membrane system at overlimiting currents*. Journal of Physical Chemistry B, 2007. **111**(51): p. 14208-14222.
10. Rubinstein, I. and L.A. Segel, *Breakdown of a Stationary Solution to the Nernst-Planck-Poisson Equations*. Journal of the Chemical Society-Faraday Transactions II, 1979. **75**: p. 936-940.
11. Rubinstein, I. and L. Shtilman, *Voltage against Current Curves of Cation-Exchange Membranes*. Journal of the Chemical Society-Faraday Transactions II, 1979. **75**: p. 231-246.
12. Rubinstein, I. and B. Zaltzman, *Electro-osmotically induced convection at a permselective membrane*. Physical Review E, 2000. **62**(2): p. 2238-2251.
13. Zaltzman, B. and I. Rubinstein, *Electro-osmotic slip and electroconvective instability*. Journal of Fluid Mechanics, 2007. **579**: p. 173-226.
14. Ouyang, W., J. Han, and W. Wang, *Nanofluidic crystals: nanofluidics in a close-packed nanoparticle array*. Lab on a Chip, 2017. **17**(18): p. 3006-3025.
15. Quake, S.R. and A. Scherer, *From micro- to nanofabrication with soft materials*. Science, 2000. **290**(5496): p. 1536-1540.
16. Dydek, E.V., et al., *Overlimiting Current in a Microchannel*. Physical Review Letters, 2011. **107**(11).
17. Cheng, L.J. and L.J. Guo, *Nanofluidic diodes*. Chemical Society Reviews, 2010. **39**(3): p. 923-938.
18. Yossifon, G., Y.C. Chang, and H.C. Chang, *Rectification, Gating Voltage, and Interchannel Communication of Nanoslot Arrays due to Asymmetric Entrance Space Charge Polarization*. Physical Review Letters, 2009. **103**(15).
19. Wang, H., et al., *Controlling the Ionic Current Rectification Factor of a Nanofluidic/Microfluidic Interface with Symmetric Nanocapillary Interconnects*. Analytical Chemistry, 2015. **87**(7): p. 3598-3605.
20. Bird, R.B., W.E. Stewart, and E.N. Lightfoot, *Transport phenomena*. Revised second edition. ed. 2007, New York: John Wiley & Sons, Inc. xii, 905 pages.
21. Cho, I., et al., *Non-Negligible Diffusio-Osmosis Inside an Ion Concentration Polarization Layer*. Physical Review Letters, 2016. **116**(25).
22. Nam, S., et al., *Experimental Verification of Overlimiting Current by Surface Conduction and Electro-Osmotic Flow in Microchannels*. Physical Review Letters,

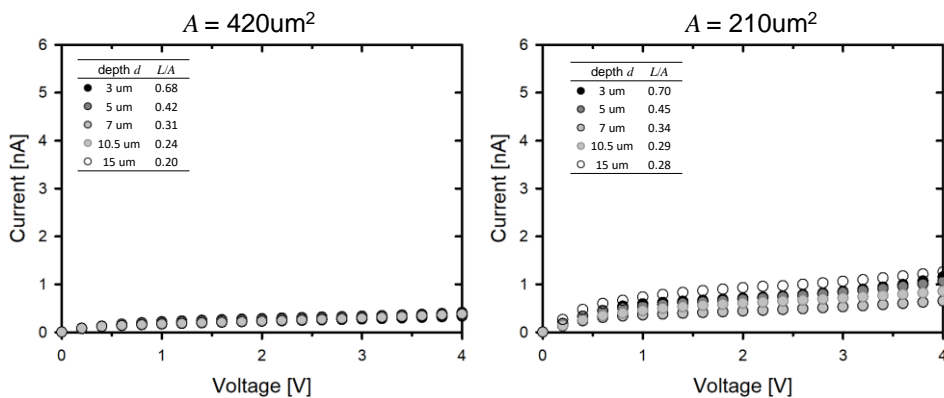
2015. **114**(11).
23. Han, J.H., et al., *Over-limiting Current and Control of Dendritic Growth by Surface Conduction in Nanopores*. Scientific Reports, 2014. **4**.
 24. Mani, A. and M.Z. Bazant, *Deionization shocks in microstructures*. Physical Review E, 2011. **84**(6).
 25. Rubinstein, I. and B. Zaltzman, *Equilibrium Electroconvective Instability*. Physical Review Letters, 2015. **114**(11).
 26. Pundik, T., I. Rubinstein, and B. Zaltzman, *Bulk electroconvection in electrolyte*. Physical Review E, 2005. **72**(6).
 27. Kwak, R., et al., *Shear Flow of an Electrically Charged Fluid by Ion Concentration Polarization: Scaling Laws for Electroconvective Vortices*. Physical Review Letters, 2013. **110**(11).
 28. Kim, W., et al., *Experimental verification of simultaneous desalting and molecular preconcentration by ion concentration polarization*. Lab on a Chip, 2017. **17**(22): p. 3841-3850.
 29. Kim, K., et al., *Stabilization of ion concentration polarization layer using micro fin structure for high-throughput applications*. Nanoscale, 2017. **9**(10): p. 3466-3475.
 30. Kim, J., et al., *Ion Concentration Polarization by Bifurcated Current Path*. Scientific Reports, 2017. **7**.
 31. Rubinstein, I., B. Zaltzman, and I. Lerman, *Electroconvective instability in concentration polarization and nonequilibrium electro-osmotic slip*. Physical Review E, 2005. **72**(1).
 32. Kim, P., et al., *Stabilization of Ion Concentration Polarization Using a Heterogeneous Nanoporous Junction*. Nano Letters, 2010. **10**(1): p. 16-23.
 33. Kim, S.J., et al., *Multi-vortical flow inducing electrokinetic instability in ion concentration polarization layer*. Nanoscale, 2012. **4**(23): p. 7406-7410.
 34. Lee, H., et al., *A concentration-independent micro/nanofluidic active diode using an asymmetric ion concentration polarization layer*. Nanoscale, 2017. **9**(33): p. 11871-11880.
 35. Deng, D.S., et al., *Water purification by shock electrodialysis: Deionization, filtration, separation, and disinfection*. Desalination, 2015. **357**: p. 77-83.
 36. Deng, D.S., et al., *Overlimiting Current and Shock Electrodialysis in Porous Media*. Langmuir, 2013. **29**(52): p. 16167-16177.
 37. Yaroshchuk, A., *Over-limiting currents and deionization "shocks" in current-induced polarization: Local-equilibrium analysis*. Advances in Colloid and Interface Science, 2012. **183**: p. 68-81.
 38. Mirzadeh, M., F. Gibou, and T.M. Squires, *Enhanced Charging Kinetics of Porous Electrodes: Surface Conduction as a Short-Circuit Mechanism*. Physical Review Letters, 2014. **113**(9).
 39. Duffy, D.C., et al., *Rapid prototyping of microfluidic systems in poly(dimethylsiloxane)*. Analytical Chemistry, 1998. **70**(23): p. 4974-4984.
 40. Cho, I., G.Y. Sung, and S.J. Kim, *Overlimiting current through ion concentration polarization layer: hydrodynamic convection effects*. Nanoscale, 2014. **6**(9): p. 4620-4626.
 41. Choi, J., et al., *Selective preconcentration and online collection of charged molecules using ion concentration polarization*. Rsc Advances, 2015. **5**(81): p. 66178-66184.
 42. Son, S.Y., et al., *Engineered Nanofluidic Preconcentration Devices by Ion Concentration Polarization*. Biochip Journal, 2016. **10**(4): p. 251-261.
 43. Kim, J., et al., *Pseudo 1-D Micro/Nanofluidic Device for Exact Electrokinetic Responses*. Langmuir, 2016. **32**(25): p. 6478-6485.
 44. Yan, D., et al., *Theory of linear sweep voltammetry with diffuse charge: Unsupported electrolytes, thin films, and leaky membranes*. Physical Review E, 2017. **95**(3).

45. Andersen, M.B., et al., *Confinement effects on electroconvective instability*. *Electrophoresis*, 2017. **38**(5): p. 702-711.
46. Nikonenko, V.V., et al., *Desalination at overlimiting currents: State-of-the-art and perspectives*. *Desalination*, 2014. **342**: p. 85-106.
47. Kwak, R., et al., *Microscale electro dialysis: Concentration profiling and vortex visualization*. *Desalination*, 2013. **308**: p. 138-146.
48. Lee, S.H., et al., *Sub-10 nm transparent all-around-gated ambipolar ionic field effect transistor*. *Nanoscale*, 2015. **7**(3): p. 936-946.
49. Alizadeh, S. and A. Mani, *Multiscale Model for Electrokinetic Transport in Networks of Pores, Part I: Model Derivation*. *Langmuir*, 2017. **33**(25): p. 6205-6219.
50. Alizadeh, S. and A. Mani, *Multiscale Model for Electrokinetic Transport in Networks of Pores, Part II: Computational Algorithms and Applications*. *Langmuir*, 2017. **33**(25): p. 6220-6231.
51. Lee, K., et al., *Enhancing the sensitivity of DNA detection by structurally modified solid-state nanopore*. *Nanoscale*, 2017. **9**(45): p. 18012-18021.
52. Xu, S., et al., *Soft Microfluidic Assemblies of Sensors, Circuits, and Radios for the Skin*. *Science*, 2014. **344**(6179): p. 70-74.
53. Kim, D.H., et al., *Epidermal Electronics*. *Science*, 2011. **333**(6044): p. 838-843.
54. Kim, C.C., et al., *Highly stretchable, transparent ionic touch panel*. *Science*, 2016. **353**(6300): p. 682-687.
55. Cheow, L.F., et al., *Detecting Kinase Activities from Single Cell Lysate Using Concentration-Enhanced Mobility Shift Assay*. *Analytical Chemistry*, 2014. **86**(15): p. 7455-7462.
56. Ko, S.H., et al., *Massively parallel concentration device for multiplexed immunoassays*. *Lab on a Chip*, 2011. **11**(7): p. 1351-1358.
57. Ko, S.H., et al., *Nanofluidic preconcentration device in a straight microchannel using ion concentration polarization*. *Lab on a Chip*, 2012. **12**(21): p. 4472-4482.
58. Hong, S.A., et al., *Electrochemical detection of methylated DNA on a microfluidic chip with nanoelectrokinetic pre-concentration*. *Biosensors & Bioelectronics*, 2018. **107**: p. 103-110.
59. Choi, E., et al., *High Current Ionic Diode Using Homogeneously Charged Asymmetric Nanochannel Network Membrane*. *Nano Letters*, 2016. **16**(4): p. 2189-2197.
60. Jung, J.Y., et al., *Electromigration Current Rectification in a Cylindrical Nanopore Due to Asymmetric Concentration Polarization*. *Analytical Chemistry*, 2009. **81**(8): p. 3128-3133.
61. Kim, B., et al., *Tunable Ionic Transport for a Triangular Nanochannel in a Polymeric Nanofluidic System (vol 7, pg 740, 2013)*. *Acs Nano*, 2013. **7**(9): p. 8311-8311.
62. Perazzo, A., et al., *Tuning crystal structure in a micro-scale reactive flow*. *Chemical Engineering Science*, 2019. **207**: p. 581-587.
63. Goh, P.S., et al., *Membrane fouling in desalination and its mitigation strategies*. *Desalination*, 2018. **425**: p. 130-155.
64. Chang, I.S., et al., *Membrane fouling in membrane bioreactors for wastewater treatment*. *Journal of Environmental Engineering*, 2002. **128**(11): p. 1018-1029.
65. Meng, F.G., et al., *Recent advances in membrane bioreactors (MBRs): Membrane fouling and membrane material*. *Water Research*, 2009. **43**(6): p. 1489-1512.
66. Meng, S., et al., *Fouling and crystallisation behaviour of superhydrophobic nanocomposite PVDF membranes in direct contact membrane distillation*. *Journal of Membrane Science*, 2014. **463**: p. 102-112.
67. Andritsos, N., et al., *Calcium carbonate deposit formation under isothermal conditions*. *The Canadian Journal of Chemical Engineering*, 1996. **74**(6): p. 911-919.
68. Shirazi, S., C.-J. Lin, and D. Chen, *Inorganic fouling of pressure-driven membrane processes—A critical review*. *Desalination*, 2010. **250**(1): p. 236-248.

69. Filloux, E., et al., *Biofouling and scaling control of reverse osmosis membrane using one-step cleaning-potential of acidified nitrite solution as an agent*. Journal of Membrane Science, 2015. **495**: p. 276-283.
70. Zhang, J., et al., *Synergetic effects of oxidized carbon nanotubes and graphene oxide on fouling control and anti-fouling mechanism of polyvinylidene fluoride ultrafiltration membranes*. Journal of Membrane Science, 2013. **448**: p. 81-92.
71. Warsinger, D.M., et al., *Scaling and fouling in membrane distillation for desalination applications: A review*. Desalination, 2015. **356**: p. 294-313.
72. Belova, E.I., et al., *Effect of anion-exchange membrane surface properties on mechanisms of overlimiting mass transfer*. Journal of Physical Chemistry B, 2006. **110**(27): p. 13458-13469.
73. Simons, R., *Water Splitting in the Cell-Membrane - Possible Effects on Membrane Conductance and Intracellular Pressure*. Biochimica Et Biophysica Acta, 1985. **813**(1): p. 145-147.
74. Lee, H., et al., *Overlimiting current in non-uniform arrays of microchannels*. 2019.

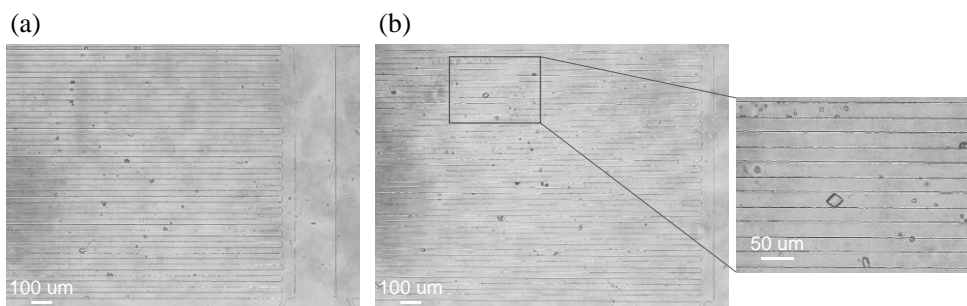
Appendix

For the full data set of I-V response, Appendix Figure 1 was given for the cases of $A = 420 \text{ um}^2$ and $A = 210 \text{ um}^2$, followed by the Figure 6(a), (b) and (c).

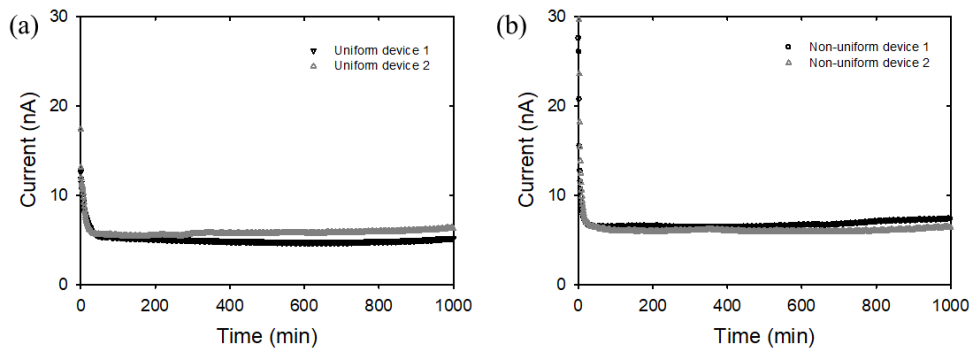


Appendix Figure 1. Additional data set of Figure 6.

Appendix Figure 2 shows the micrographs of the Ca(OH)_2 crystals formed inside the microchannels. The crystals were formed from CaCl_2 electrolyte inside the main microchannels when a constant voltage was applied for 1000 minutes.



Appendix Figure 2. Additional figures of Figure 12. Crystals formed in uniform array devices filled with CaCl_2 electrolyte. (a) 5 V was applied for 1000 minutes (b) 10 V was applied for 1000 minutes.



Appendix Figure 3. Current responses under constant voltage of 5 V from (a) uniform array devices and (b) non-uniform array devices. The electrolyte was 1 mM KCl in both cases.

Abstract in Korean

전기동역학적 관점에서 연구된 마이크로 채널의 이온 전류 현상은 새로운 마이크로/나노 유체 장치로 응용되며 상당한 관심을 받아왔다. 현재까지 제기된 다양한 이온 전달 방식 중, 표면 전도 (Surface conduction, SC)는 마이크로/나노 유체 장치의 주요 메커니즘으로서 2차원 분석에 기초하여 이론적으로 묘사되었다. 하지만 기존 접근 방식에서 하나 이상의 축을 무한으로 가정한 것은 이론 연구 결과를 실제 마이크로/나노 채널 네트워크에 적용 할 때 불일치를 야기하였다. 따라서 본 논문에서는 채널의 3차원 길이 요소를 모두 포함한 실험 연구를 진행하였다. 유체 장치의 과제한 전기전도도 (Overlimiting conductance, OLC)는 채널의 단면적이 일정할 때 둘레 길이가 커질수록 증가하였는데 이는 비표면적이 커질수록 이온 수송량이 증가한다는 것을 의미한다. 따라서 실험 결과는 표면 전도의 존재를 뚜렷하게 보여주었으며, 표면 전도가 지배적인 영역에서 채널의 둘레 길이와 단면적의 비율 (L/A , L : 둘레의 길이, A : 단면적)이 이온 수송을 정량적으로 해석하기 위한 단일 변수로 제시되었다. 이를 이용해 L/A 를 비대칭적으로 조절한 마이크로 채널에 전압을 인가하여 정류 효과를 관측하였다. 나아가 마이크로 채널 네트워크의 이온 전도 전류의 안정성을 보장하기 위한 연구를 진행하였다. 미세 채널 내에서 생성된 부산물 또는 축적된 입자들은 유체 기반 장치에서 비가역적인 기능 저하를 일으킬 수 있다. 특히 바닷물의 담수화와 같이 전해용액이 칼슘 이온을 포함할 경우 수산화칼슘 결정이 생성될 수 있고 이는 채널의 이온 전류 흐름을 방해 또는 차단하는 문제를 발생시킨다. 따라서 두

번째 장에서는 채널 네트워크에 기하학적 비균일성을 적용하여 이러한 결정화를 효과적으로 제어할 수 있음을 보였다. 균일한 배열을 가진 평행 마이크로 채널 시스템과 비교하여 채널의 폭에 비균일한 변화가 있을 때 유체 내 재순환 (recirculation) 흐름이 강화되는 것을 관측하였다. 이러한 흐름 양상은 결정 생성의 원인이 되는 채널 내 국소적인 이온 농축을 최소화하여 시스템의 전류 흐름을 안정적으로 유지하는 데 기여한다. 위 연구들은 마이크로/나노 장치 설계의 가이드라인을 제시하며 마이크로 채널 간 유체 흐름을 이용해 외부 에너지의 유입 없이 시스템의 작동 수명을 확보하는 실용적인 방안이 될 것으로 기대된다.

주요어 : 이온농도분극현상, 표면 전도, 비균일성, 결정 생성 방지.

학번 : 2018-20846

Acknowledgements

My master's course at Seoul National University was extremely rich for me. I have a lot of people to thank for having made my study and work so lively and productive.

First of all, I would like to express my deepest gratitude to my supervisor, Prof. Sung Jae Kim for giving me an opportunity to join the EES laboratory since I was an undergraduate. I would like to appreciate his expertise, patience, and guidance during my long journey in the lab. I would also like to acknowledge my debt to Dr. Inhee Cho for supporting my project from scratch. This work could not have been completed without their dedicated support and counsel. My sincere gratitude also goes to Prof. Hyomin Lee for kindly reviewing my work and giving detailed and constructive comments. During this work, I have collaborated with many colleagues for whom I have great regard, and I wish to extend my warmest thanks to all those who have supported me. Their knowledge and skill were necessary to choose the right direction, obtain good results, and broaden my knowledge. I could not have overcome the difficulties and completed the course without them.

Last but not the least, my sincere gratitude to my family, especially to my parents and my sister for the constant encouragement and care they provided me throughout my entire life.